Bioinspiration & Biomimetics

PAPER

Numerical investigation of low-noise airfoils inspired by the down coat of owls

RECEIVED
23 July 2018

REVISED
1 November 2018

ACCEPTED FOR PUBLICATION
16 November 2018

PUBLISHED
6 December 2018

Andrew Bodling[1] **and Anupam Sharma**[2]

Department of Aerospace Engineering, Iowa State University, Ames, IA 50011, United States of America

[1] PhD candidate, 1200 Howe Hall, Ames IA, 50011. AIAA Student Member.

[2] Associate Professor, 2341 Howe Hall, Ames, IA, 50011. AIAA Associate Fellow.

E-mail: abodling@iastate.edu **and** sharma@iastate.edu

Keywords: large eddy simulations, low noise airfoils, night owl

Abstract

Numerical analysis of airfoil geometries inspired by the down coat of the night owl is presented. The bioinspired geometry consists of an array of 'finlet fences', which is placed near the trailing edge of the baseline (NACA 0012) airfoil. Two fences with maximum nondimensional heights, $H/\delta^* = 1$ and 2.26 are investigated, where δ^* is the displacement thickness at 2.9% chord upstream of the airfoil trailing edge. Wall-resolved large eddy simulations are performed at chord-based Reynolds number, $Re_c = 5 \times 10^5$, flow Mach number, $M = 0.2$, and angle of attack, $\alpha = 0°$. The simulation results show significant reductions in unsteady surface pressure and farfield radiated noise with the fences, in agreement with the measurements available in the literature. Analysis of the results reveals that the fences increase the distance between the boundary layer turbulence (source) and the airfoil trailing (scattering) edge, which is identified to be the mechanism behind high-frequency noise reduction. These reductions are larger for the taller fence as the source-scattering edge separation is greater. Two-point correlations show that the fences reduce the spanwise coherence at low frequencies for separation distances greater than a fence pitch (distance between two adjacent fences) and increase the coherence for smaller distances, the increase being higher for the taller fence. This increase in coherence and the reduced obliqueness of the leading edge of the fence are hypothesized to be responsible for the small increase in farfield noise at low frequencies observed in the simulations with the taller fence.

1. Introduction

Noise generated due to fluid flow and its interaction with solid surfaces is termed aerodynamic noise. Aerodynamic noise due to the interaction of the turbulence in the boundary layer over a blade with the blade surface is often referred to as 'self' noise [1]. Self noise can be generated via different mechanisms: separation stall noise, laminar boundary layer-vortex shedding noise, tip vortex formation noise and trailing edge noise. This paper focuses on trailing edge noise; specifically on its mitigation through bioinspired blade designs.

Trailing edge noise is broadband in nature and is generated by scattering of the hydrodynamic energy in a turbulent boundary layer into acoustic radiation. The turbulent fluctuations in the boundary layer can radiate sound directly (with a sound power scaling of M^8, where M is the flow Mach number), but it is their close proximity to the airfoil surface that amplifies the sound produced in subsonic flow (sound power scaling becomes M^6) [2]. This amplification is due to the unsteady surface pressure on the airfoil surface (generated by the turbulent boundary layer) which radiates more efficiently than free turbulence when the flow Mach number is small ($\leqslant$0.2). Furthermore, when the surface has a singularity, such as at the airfoil leading and trailing edges, the sound radiation becomes even more efficient (sound power scaling of M^5) [3–5]. Trailing edge noise is therefore a dominant noise source in blades operating in clean flow (low inflow turbulence) at low Mach number. These conditions are realized in wind turbine blades [6], civil aircraft during approach and takeoff, underwater vehicles [7], household fans, HVAC blowers, etc. The long term goal of the aviation industry to reduce aircraft noise by 20 dB [8] cannot be achieved without mitigating trailing edge noise. Growth of the wind energy industry is also

© 2018 IOP Publishing Ltd

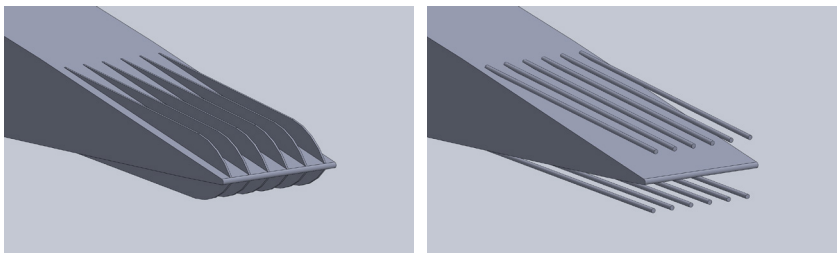

(a) (b)

Figure 1. Idealized representations of the (a) finlet fence and (b) finlet rail designs which were experimentally investigated in [26]. The struts to support the finlet rails are omitted for clarity.

curtailed due to the annoyance caused by rotor blade noise, which is predominantly trailing edge noise.

A variety of innovative technologies have been developed using biomimicry [9], e.g. self-cleaning paints using the lotus leaf effect [10], temperature-regulated buildings inspired by termite mounds [11], etc. Nature has also provided a solution for silent flight in night owls [12, 13]. Night owls require the acoustic stealth to avoid aural detection by the prey and also to aurally locate their prey in the dark [14]. A night owl can not be heard until it is within three meters of its prey [15]. One species of night owls—the barn owl (*Tyto alba*)—is particularly skilled at silent flight. Hereinafter, we shall refer to the barn owl as 'the owl'. While this biological marvel has been known to mankind for almost a century, it is yet to find its due engineering application.

Previous investigations [12, 13, 15] have found three important anatomical features that presumably play a role in reducing noise during owl flight. These features are collectively referred to as the owl 'hush kit'. The hush kit comprises of:

1. A stiff comb-like structure (referred as serrations) at the leading edge (LE) of the wing,
2. A flexible fringe like structure at the trailing edge (TE) of the wing, and
3. A soft, thick down coat on the flight feathers.

It is emphasized that the chord-based Reynolds number for the owl in flight is between 50 000–90 000. The applications of interest, such as aircraft wings and wind turbine blades, operate at much higher Reynolds number. The objective therefore is to take inspiration from the night owl, rather than replicate its anatomy, to design ultra-quiet blade designs.

Owl-inspired LE and TE designs (serrations) have been developed and investigated extensively in laboratory [16–19] and in the field [20]. This paper focuses on the third owl feather feature in the list above—the down coat, which has not received as much research attention until recently. Geyer *et al* [21] related the down coat to the porosity of a wing. By doing a series of experiments that used airfoils made out of different porosity materials, they found that at the frequencies less than about 10 kHz, porous airfoils were able to attenuate the trailing edge broadband noise by over 10 dB. However, the aerodynamic performance decreased as the resistivity of the airfoils increased with porosity. Jaworski and Peake [22, 23] analyzed the trailing-edge condition and found that the fifth-power (M^5) dependency of the radiated acoustic power of a trailing edge was weakened by both porosity and flexibility. However, they did not investigate the effect of the feather structure formed by the hairs on the flight feathers of the owl.

Microscopic observations by Clark *et al* [24] revealed that hairs on owl feathers rise vertically up from the feather substrate (lifting surface of the wing) and then plateau out in the streamwise direction, forming a structure similar to a forest/plant canopy [24]. Fluid flow in plant canopies has been investigated elsewhere [25]. Clark *et al* [24] found that the owl canopy has an open area ratio of about 70% and is is suspended approximately 0.5 mm above the feather substrate. Based on these observations, they designed artificial canopies with different open area ratios and performed wall-jet wind tunnel experiments to examine the effect of the canopies on surface roughness noise. The canopies were designed using a large number of parallel fibers made from the material used for fishing lines. These fibers were oriented in the direction of the flow and located just above the flow surface. The canopies were found to reduce both the surface pressure fluctuations (by as much as 30 dB!) and the radiated farfield noise.

This exciting discovery motivated them to develop trailing edge noise reduction designs. These designs also used the concept of canopy, but were designed to be robust enough for industrial application, e.g. on wind turbine blades. The designs presented in Clark *et al* [26] achieved the canopy effect by attaching small structures (height less than the boundary layer) near the trailing edge, which they called 'finlets'. Figure 1 shows schematics of two finlet designs, finlet fence and finlet rail, used in these experiments. Twenty different configurations of these two designs were tested in the experiments by changing the height, spacing, thickness, and extension of the fences and rails. Compared to the unmodified (baseline) airfoil, these configurations were found to reduce the trailing edge noise by up to 10 dB [26].

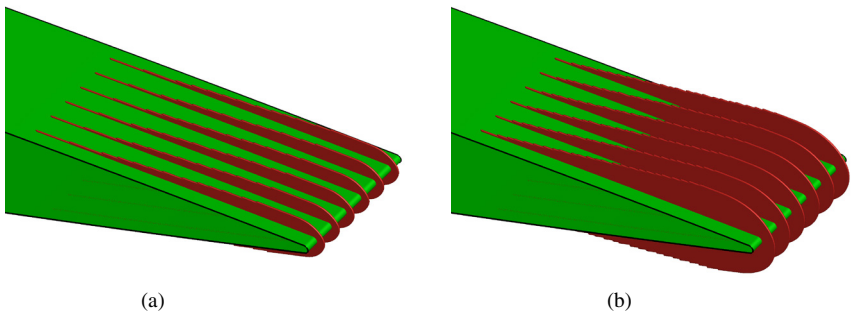

(a) (b)

Figure 2. Geometry of the two fence configurations used in the simulations with maximum normalized fence heights, $H/\delta^* =$ (a) 1.0 and (b) 2.26. The maximum fence height occurs at $x/c = 0.971$.

Based on the results of the different configurations tested, the finlets are believed to: (a) lift the energetic eddies in the turbulent boundary layer away from the airfoil trailing edge, thereby reducing the scattering efficiency, and (b) reduce spanwise coherence in the boundary layer. These are the working hypotheses behind the observed noise reduction. The objective of this paper is to use high-fidelity aeroacoustics simulations to determine the mechanisms behind the observed noise reduction to verify or disprove the working hypotheses.

Highly-resolved large eddy simulations are conducted for the baseline airfoil (NACA 0012) as well as the baseline airfoil fitted with two different fence finlet designs. It should be noted that the baseline airfoil in the experiments of [26] was different. The experiments used the DU96-W-180 airfoil, which is commonly used in the design of the tip section of utility scale wind turbines. Furthermore, the simulations are performed at a smaller Reynolds number compared to the experiments—$Re_c^{(\mathrm{sim})} = 5 \times 10^5$ versus $Re_c^{(\mathrm{exp})} = 2.5 \times 10^6$. These simplifications are made to manage the computational complexity of the problem; the intent here is to focus on the physical phenomena behind noise reduction rather than perform a direct validation (one-to-one comparison) with the experimental data. Nevertheless, the simulations reveal several interesting flow physics that shed new light on the physical mechanisms behind the observed noise reduction.

This research builds upon authors' recent work in simulating fence finlets [27–29]. Bodling *et al* [29] investigated the aeroacoustic impact of the shape of the leading edge of the finlet fences and found that it has to be highly skewed (oblique incidence) to the incoming flow to achieve noise reduction. They also noted that the fence finlets indeed increase the separation distance between the energetic turbulent eddies and the airfoil trailing (scattering) edge. In this article, we study the effect of varying the height of the finlet fences to bolster our understanding of the noise reduction mechanisms. Results from three sets of simulations are presented and compared: baseline airfoil, and baseline airfoil fitted with two fence finlets with maximum fence heights $H/\delta^* = 1$ and 2.26, where δ^* is the displacement thickness at 2.9% chord upstream of the airfoil trailing edge. Displacement thickness is chosen as the reference length scale for noise analysis as the main mechanism of noise reduction is believed to be displacement of energetic turbulent eddies away from the airfoil trailing edge. Figure 2 shows the two fence finlet geometries used in the simulations. Given the differences in the airfoil geometries between the simulations and the fence finlets experiment [26], the comparisons are drawn to test for *trend* prediction rather than a quantitative verification; absolute validation against aerodynamic measurements for the baseline airfoil are presented in the paper to demonstrate solver accuracy. The objective is to perform source diagnostics using the highly-resolved flowfield to enhance our understanding of the mechanisms behind the noise reduction observed with finlets.

2. Numerical methodology

The aeroacoustic performance of the baseline and finlet fence models is evaluated using a two-step approach. First, the unsteady flow around the geometry is simulated using a computational fluid dynamics (CFD) solver; time-accurate flow data is collected during the CFD simulation on a surface enclosing the airfoil and the sound sources. In the second step, the surface data is used with an integral method (acoustic analogy) to predict the farfield noise radiation. The numerical procedure used in this work has been previously validated and used to assess the noise reduction ability of leading edge serrations [19] and finlets [27–29].

2.1. Compressible flow solver

Aeroacoustics simulations require resolution of wide ranges of spatial, temporal, and energy scales because of the requirement to simultaneously compute hydrodynamic and acoustic fields in the flow. Very high accuracy is therefore required of such solvers even when they are coupled with integral methods for farfield noise prediction as the solver still has to accurately compute the tiny acoustic perturbations alongside the unsteady hydrodynamic field. For the present work, the compressible Navier–Stokes solver, FDL3DI [30], is used for the flow simulations. FDL3DI

solves the full unfiltered compressible Navier–Stokes equations on curvilinear meshes. The governing fluid flow equations, after performing a time-invariant curvilinear coordinate transform $(x, y, z) \rightarrow (\xi, \eta, \zeta)$, are written in a strong conservation form as

$$\frac{\partial}{\partial t}\left(\frac{\mathbf{U}}{J}\right) + \frac{\partial \hat{\mathbf{F}}_I}{\partial \xi} + \frac{\partial \hat{\mathbf{G}}_I}{\partial \eta} + \frac{\partial \hat{\mathbf{H}}_I}{\partial \zeta} = \frac{1}{Re}\left[\frac{\partial \hat{\mathbf{F}}_v}{\partial \xi} + \frac{\partial \hat{\mathbf{G}}_v}{\partial \eta} + \frac{\partial \hat{\mathbf{H}}_v}{\partial \zeta}\right], \tag{1}$$

where J is the Jacobian of the coordinate transformation, $\mathbf{U} = \{\rho, \rho u, \rho v, \rho w, \rho E\}$; the expressions for the inviscid flux terms, $\hat{\mathbf{F}}_I, \hat{\mathbf{G}}_I, \hat{\mathbf{H}}_I$, and the viscous flux terms, $\hat{\mathbf{F}}_v, \hat{\mathbf{G}}_v, \hat{\mathbf{H}}_v$, are available in [30].

The *implicit* large eddy simulation (LES) approach is used for the simulations. Unlike traditional LES, the governing equations are not filtered. As a result, there are no additional sub-grid stress terms to model the dissipation of the unresolved, small-scale flow structures. These sub-grid flow structures are removed (filtered out) from the solution by applying discriminating, high-order (up to 10th order), low-pass spatial filters to the conserved flow variables. The filter is discriminating in the sense that it only removes wavenumbers that cannot be resolved by the grid. The filtering procedure is applied after each timestep. The implicit LES approach effectively becomes direct numerical solution (DNS) in the limit of grid refinement reaching the Kolmogrov scale.

The filter used in the interior nodes has the following stencil,

$$\alpha_f \hat{\phi}_{i-1} + \hat{\phi}_i + \alpha_f \hat{\phi}_{i+1} = \sum_{n=0}^{N} \frac{a_n(\phi_{i-n} + \phi_{i+n})}{2}, \tag{2}$$

where α_f is the free parameter that provides some control on the 'degree' of filtering, ϕ is the solution before filtering, $\hat{\phi}$ is the filtered solution, a_n is the set of coefficients for a given order of accuracy of the filter and $2N$ is the order of accuracy of the filter which has a stencil of $2N + 1$ points. An 8th-order filter with $\alpha_f = 0.45$ is applied on the interior nodes in the simulations presented here. One sided filters are used at the boundaries. Details of the filtering strategy used at boundaries are discussed in Bodling [31].

To discretize the spatial domain, up to sixth-order accurate compact finite difference schemes are used. Time integration is performed using the second-order accurate Beam–Warming implicit scheme [32, 33]. The FDL3DI solver uses the overset (Chimera) mesh approach to handle complex geometries where the fluid domain can be discretized using multiple overlapping blocks. High-order (10th) interpolation is used for communication between the blocks to maintain the spectral-like accuracy of the solver. A 5-point overlap is used to enable 10th-order interpolation. The decomposed grid is solved in parallel using a hybrid MPI-OpenMP approach; MPI refers to message passing interface. Message passing is used with domain decomposition for data parallelism, and multithreading is used to further boost the parallel performance of the software on multi-core processors.

2.2. Prediction of Farfield noise

Farfield sound propagation is performed using the Ffowcs Williams–Hawkings (FW-H) acoustic analogy [34]. By neglecting volume sources (valid for low Mach number flows), the following integral equation is obtained for far-field acoustic pressure, p' at location $\mathbf{x}$ and time t:

$$p'(\boldsymbol{x}, t) = \frac{1}{4\pi\,|1 - M_r|\,|\boldsymbol{x}|}\left(\frac{\partial}{\partial t}\int\int [\rho_0 u_i n_i + \rho'(u_i - U_i)n_i]\mathrm{d}\Sigma + \frac{x_i}{c\,|\boldsymbol{x}|}\frac{\partial}{\partial t}\int\int [p' n_i + \rho u_i(u_j - U_j)n_j]\mathrm{d}\Sigma\right). \tag{3}$$

Solving equation (3) requires integrating over a surface Σ that encloses all sound sources. In the above, n_i is normal to the surface Σ, p' and ρ' are pressure and density fluctuations, ρ_0 is mean density, u_i is perturbation flow velocity and U_i is the velocity of the surface Σ. The source is at the origin, and $\boldsymbol{x}$ denotes the observer location. We choose a 'porous' surface around the airfoil defined by one of the gridlines ($\xi =$ constant >1; $\xi = 1$ is the airfoil surface) of the grid block. The FW-H solver has been validated previously against canonical problems (point monopole, dipole, and quadrupole) as well as against experimental data for aerodynamic noise from propellers [35]. The FW-H solver has also been verified against computational results for point sources in a moving medium [31, 36].

2.3. Kato's correction

The span of the airfoil in the simulations, S_s is less than the span of the airfoil used in the experiments, S_e of [26]. Therefore, the predicted farfield noise needs to be corrected before comparing to the experimental data. The correction depends on the spanwise coherence length L_c. When the coherence length is less than the simulated span, as is the case for the simulations presented here, the following equation is used to compare the measured and predicted farfield sound spectra S_{pp}.

$$(S_{pp}(\omega))_e = (S_{pp}(\omega))_s + 10\log(S_e/S_s), \quad L_c < S_s < S_e. \tag{4}$$

Equation (4) assumes that over the span length of L_c there is perfect correlation, and outside of this length the correlation drops identically to zero. This 'box-car' simplification by Kato and Ikegawa [37] is often used in such aeroacoustic predictions.

3. Geometry modeling, meshing, and boundary conditions

The NACA0012 airfoil is selected as the baseline airfoil. For the bioinspired airfoil, finlet fences are added near the airfoil trailing edge. The span length of all the models in the simulations is 5.85% of the airfoil

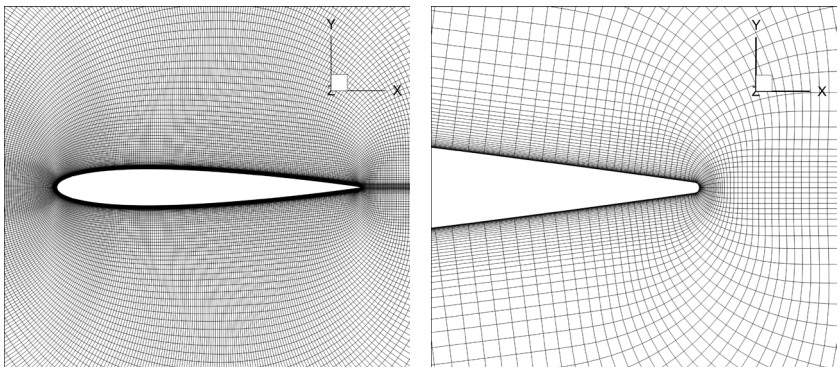

(a) (b)

Figure 3. O-grid topology of the baseline mesh used in the simulation. The trailing edge is rounded and the mesh near the TE is shown in (b). Every fourth point along each axis is shown for clarity. (a) Baseline mesh (b) Baseline mesh near the TE.

chord. Two-point correlation analysis presented in [29] demonstrated that this span length is adequate to ensure that the sound sources radiate independently.

A single-block, O-grid is used to generate a 2D mesh around the baseline airfoil, which is repeated in the span direction to obtain the 3D grid. The near-wall mesh is obtained by normal extrusion from the airfoil surface with a high degree of refinement near the walls. The O-grid in the physical space (x, y, z) maps to an H-grid in the computational domain (ξ, η, ζ). The following orientation is used: $\hat{\boldsymbol{e}}_\xi$ points radially out, $\hat{\boldsymbol{e}}_\eta$ is in the circumferential direction, and $\hat{\boldsymbol{e}}_\zeta$ is along the span direction following the right hand rule, $\hat{\boldsymbol{e}}_\zeta = \hat{\boldsymbol{e}}_\xi \times \hat{\boldsymbol{e}}_\eta$. In the baseline grid used in this study, the O-grid distribution on the z-constant planes is similar to that described in [38], which was a LES of flow over an airfoil at $Re_c = 5 \times 10^5$. Based on the mesh sensitivity study performed in [38] and the recommendations from Georgiadis *et al* [39], the grid spacing on the suction side was found to be appropriate for LES. In the work from [38], only the suction side was resolved. Therefore, to create the grid used in this study, the suction side of the grid from [38] was mirrored in order to resolve both sides of the airfoil.

Periodic boundary condition is used in the span ($\hat{\boldsymbol{e}}_\zeta$) and azimuthal ($\hat{\boldsymbol{e}}_\eta$) directions using overset grid with five-point overlaps. The airfoil surface is modeled as a no-slip, adiabatic wall with a zero-normal pressure gradient (4th-order extrapolation). The outer computational domain boundary is approximately 110 chords away from the airfoil and is prescribed as a freestream boundary. The grid is heavily stretched away from the airfoil such that the filtering procedure annihilates all fluctuations before they reach the outer boundary and avoids spurious reflections. The computational time step, $\Delta\tau = \Delta t\, U_\infty/c$ is chosen to be small $(= 4 \times 10^{-5})$ to provide sufficient temporal resolution of the fine-scale features. In the above, c is airfoil chord, t is the dimensional time, and U_∞ is the freestream flow speed.

Table 1. The baseline grid dimensions and non-dimensional cell sizes in wall units. Average and max values are obtained over the turbulent flow region.

$N_\xi \times N_\eta \times N_\zeta$	Δy^+ avg, max	Δx^+ avg, max	Δz^+ avg, max
$410 \times 1937 \times 101$	0.567, 0.665	28.7, 37.1	14.9, 17.3

3.1. Baseline airfoil mesh

The baseline geometry is a NACA 0012 airfoil with a rounded trailing edge with $h/\delta^* \approx 0.3$, where h is the thickness of the trailing edge. According to Blake [7], this corresponds to a blunt trailing edge. The simulations are carried out at chord-based Reynolds number, $Re_c = 5 \times 10^5$, angle of attack, $\alpha = 0°$, and flow Mach number, $M_\infty = 0.2$. The choice of the first cell height with these flow conditions gives an average y^+ of 0.567 for the baseline geometry. The turbulent boundary layer is well resolved. As an example, the boundary layer at $x/c = 0.85$ contains 110 grid points with approximately 15 points in the viscous sublayer. The maximum grid stretching ratio at the top of the boundary layer is 1.04. Figure 3 shows close-up, cross-sectional views of the baseline O-grid. For clarity, every fourth point in the radial and circumferential direction is shown in figure 3.

Table 1 provides the grid dimensions and first non-dimensional cell sizes in wall units averaged over the turbulent flow region. The cell sizes are also averaged along the span. Typical values of cell sizes used in previous wall-resolved LES available in the literature are $50 \leqslant \Delta x^+ \leqslant 150$, $y^+_{wall} < 1$,$15 \leqslant \Delta z^+ \leqslant 40$, where x is the streamwise direction, y is the wall normal direction and z is in the spanwise/homogeneous direction [39]. The values used here (see table 1) are on the lower range of the values reported in literature.

3.2. Finlet fence geometry and mesh

The fence finlets used in the experiment are flushed with the airfoil and rise at a very shallow angle from the airfoil. Generating a structured mesh around such

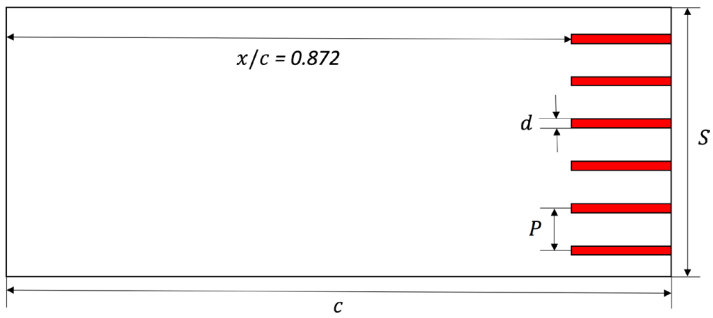

Figure 4. Schematic of the fence geometry as modeled: P is the fence pitch, d is fence thickness, c is airfoil chord length, and S is the airfoil span.

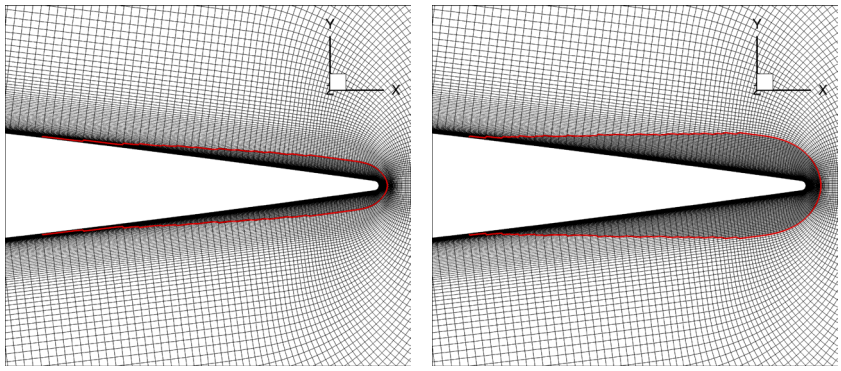

(a) (b)

Figure 5. Cross-sectional (zoom) views of the computational meshes used to simulate the $H/\delta^* = 1.0$ and $H/\delta^* = 2.26$ stair-step fence geometries. Every other grid point along each axis is shown for clarity. (a) $H/\delta^* = 1:0$. (b) $H/\delta^* = 2:26$.

a geometry while maintaining a reasonable mesh quality and manageable cell count is nearly impossible. Therefore, alternate geometry configurations are sought for which 'practical' meshes (i.e. meshes with manageable grid count and cell aspect ratios, skewness, etc that do not render the numerical algorithm unstable) can be obtained. The fences are modeled as a 'stair-step' geometry by varying the height of the fences in discrete steps (as opposed to continuous variation in the experiment model) along the chord. Such approximation of the fence geometry is justified considering that the objective is to identify the underlying flow physics behind the observed noise reduction with the fences. Note that the leading edge of each step, which is orthogonal to the oncoming turbulent flow is a scatterer of sound, is very small ($\sim$ 1%–2% of boundary layer thickness, δ) compared to the size of the energy-containing turbulent eddies ($\sim\delta$). Therefore any impact of such a stair-case representation of the fence geometry is limited to very small eddies of the boundary layer turbulence which are not important in generating sound in the human-audible frequency range.

A large number of steps are used to approximate the fence geometry as a stair-step such that it closely approximates the continuous geometry of the experiment. For the smaller fence, the final height is reached over 13 discrete stair-steps. Figure 4 shows a schematic of the modeled fence geometry with a nomenclature of the key dimensions.

The meshes for the fence simulations are obtained from the baseline mesh by performing *hole-cutting* (also called point blanking). Hole-cutting involves removing mesh points that represents the interior of a solid body; fences in this case. The PEGASUS software [40] is used to perform hole-cutting. The regions occupied by the fences (defined by specifying ranges $\xi_1 - \xi_2$, $\eta_1 - \eta_2$, and $\zeta_1 - \zeta_2$) are removed (cut out) from the baseline grid and the no-slip adiabatic wall with a zero-normal pressure gradient boundary condition (4th order extrapolation) is applied to the new boundaries thus created.

Figure 5 shows cross-sectional views of the meshes for the two different fence heights; the views are zoomed in on the fence region to clearly show the geometry differences. Every other grid point along each axis is shown for clarity. The cross-sectional views are in planes where a fence is present. The grid points in the grey regions between the airfoil surface and the red curves are blanked out (removed) from FDL3DI computation. The red curves indicate the no-slip boundaries created due to hole-cutting. The fences begin at $x/c = 0.872$ (most upstream location) and reach their maximum height (H) at $x/c = 0.971$. Based on prior experiments, Clark *et al* [41] recommend that the height of the finlets should be between 25%–50% of

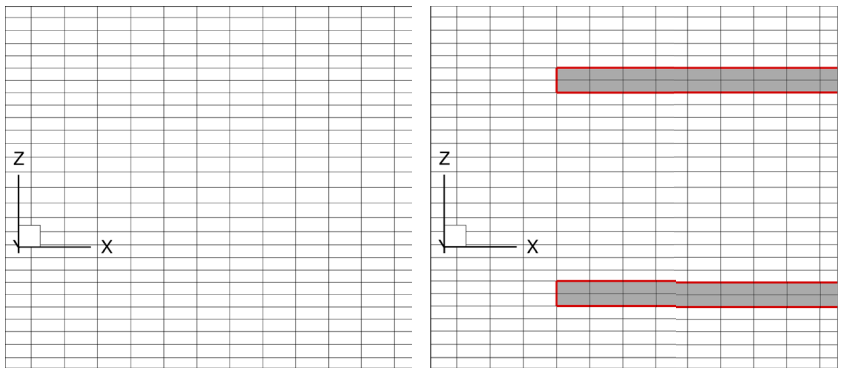

Figure 6. Top views of the baseline and fence meshes (the two fence meshes are identical from the top view). Each fence element is modeled to be two-cell thick in the simulations. (a) Baseline (b) Fence.

the boundary layer thickness. In the current simulations, the heights of the two fences are 19% and 43% of the boundary layer thickness at $x/c = 0.971$. Scaled by the displacement thickness of the baseline airfoil, the maximum nondimensional height of the two fences are $H/\delta^* = 1.0$ and 2.26. The location of the most upstream point and the location of the maximum height of the fences are the same as that used in the experiment of Clark *et al* [26].

Figure 6 shows top views of the baseline and the fence meshes (the two fence meshes appear identical in this view as only the fence height is different). Clark *et al* [41] stated that the fence thickness should be as small as possible. The fences are 2-cell thick in the current simulations, which corresponds to a nondimensional thickness $d/\delta^*(= 0.17)$. The effect of the fence spacing is not well understood, but according to Clark *et al* [41], an open area percentage of 75% or higher has been shown to yield the best performance. In the current simulations, an open area percentage of 88.5% is used, which similar to the configurations in Clark *et al* [26] that resulted in farfield noise reduction. Based on this open-area percentage, the scaled pitch (distance between two adjacent fence walls) is $P/\delta^*(= 1.49)$.

The fence meshes were not further refined in the direction normal to the fence walls as the maximum z^+ is approximately 25.2 (located at the maximum fence height), which is not significantly greater than the span-averaged baseline z^+ value near the airfoil surface. Furthermore, we are not interested is accurately resolving the boundary layer on the surfaces of the fences. Our hypothesis is that the noise is reduced due to the displacement of energy-containing turbulence eddies away from the trailing edge, which can be captured even if the fence surfaces are modeled as inviscid walls. By not resolving the boundary layer on the sides of the fence walls, we may not accurately capture some of the near-wall boundary layer flow physics, however, we believe that this level of resolution is not necessary to capture the observed noise reduction.

A mesh containing a single fence element (one fence pitch wide) is created and then repeated six times along the span to obtain a 3D mesh with a span of 5.85% chord. It should be emphasized that other than the holes introduced in the fence meshes, the grids for all three cases (baseline and two fences) are identical. This eliminates grid-to-grid differences in the simulation results when comparing the different designs.

3.3. Boundary layer trip

Since the simulation Re_c $(= 5 \times 10^5)$ is much smaller than that of the experiments $(= 2.5 \times 10^6)$, the boundary layer on the airfoil surface is forcibly tripped in the simulations. It should be noted that a boundary layer trip (serrated tape) was also used in the experiments [26]. In the simulations, boundary layer tripping is achieved by placing a geometry-resolved 'trip wire' at $x/c = 0.05$, measured from the leading edge of the airfoil. The height of the trip wire in wall units is $y^+ \sim 20$. The trip wire successfully forces the boundary layer to transition well upstream of where it would naturally transition at $Re_c = 5 \times 10^5$, thereby achieving a turbulent boundary layer similar to what would occur via natural transition at high Re_c. Details of the tripping methodology are available in [28].

3.4. Removal of transients

Several techniques are employed to reduce the computational cost of the simulations. Each simulation is initiated in 2D, with a potential flow solution as the initial condition. The Navier–Stokes equations are then solved for the 2D problem until statistical convergence is achieved; this typically takes about $10\,\tau$, where τ $(= t\,U_\infty/c)$ is the characteristic flow time. The solution is then replicated in the span direction to obtain an initial 3D solution for the baseline geometry. Transients in the 3D simulation are then removed, which takes between 3–5 τ. For the 3D simulations with fences, the solution is obtained in two steps. First the 2D solution is replicated over a single-fence span width and simulated with the fences modeled in the computation, and the solution is allowed to reach a statistical stationarity state $(\approx 10\,\tau)$. This solution is then repeated for as many

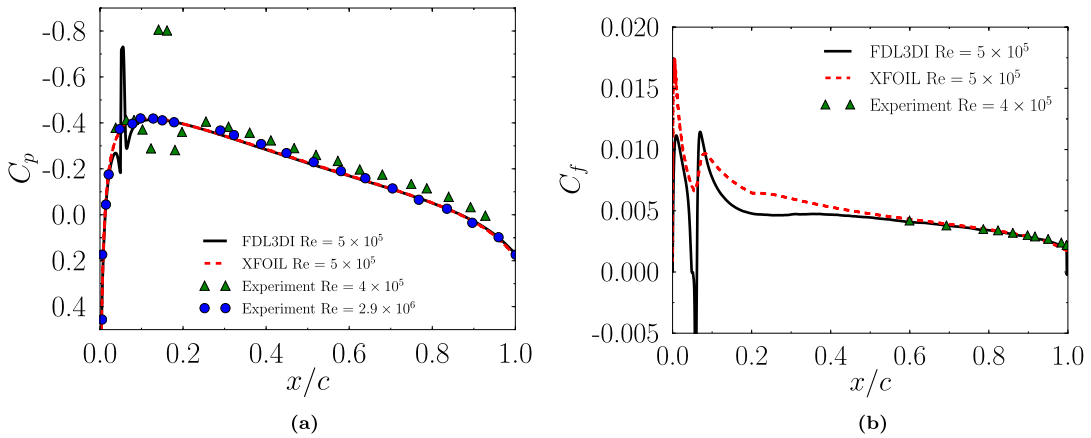

Figure 7. Time- and span-averaged C_p and C_f distributions from FDL3DI predictions ($Re_c = 5 \times 10^5$) compared with experiments ($Re_c = 4 \times 10^5$ & $Re_c = 2.9 \times 10^6$) and XFOIL simulations ($Re_c = 5 \times 10^5$). (a) Coeff. of pressure, C_p. (b) Skin friction coeff., C_f.

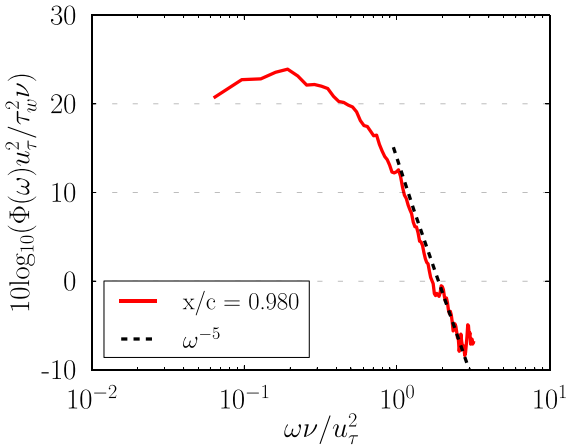

Figure 8. Predicted span-averaged surface pressure spectrum for the baseline airfoil at $x/c = 0.98$; the spectrum is normalized by the inner variables.

fences as required (= 6 here) to fit in the 5.85% span length of the full 3D geometry simulated. Transients are then removed in the full 3D simulation (with the array of fences) by simulating the flow for another 5 τ.

4. Results

This section presents the baseline validation, aerodynamic and aeroacoustic results of the numerical simulations followed by a discussion on noise reduction mechanisms with the fence designs.

4.1. Baseline validation

Once the transients are removed from the 3D simulations, the simulation data is collected for approximately 2.5 τ (≈63 000 samples) and averaged in time and along the span to compute aerodynamic performance. Figure 7(a) compares the predicted time- and span-averaged aerodynamic pressure coefficient (C_p) distributions of the baseline airfoil with experimental data and with XFOIL [42] predictions. The experimental measurements are from Sagrado *et al* [43] and Gregory *et al* [44] for NACA 0012 airfoils at $AOA = 0°$ for $Re_c = 4 \times 10^5$ and $= 2.9 \times 10^6$, respectively. The boundary layer is tripped on both surfaces of the airfoil at $x/c = 0.127$ in Sagrado *et al* [43] and at $x/c = 0.05$ in Gregory *et al* [44]. XFOIL results are also obtained with the boundary layer tripped at $x/c = 0.05$ and $Re_c = 5 \times 10^5$, which is the same as in the FDL3DI simulation. The FDL3DI prediction of C_p agrees very well with the measured data over the entire airfoil except for the notch in the FDL3DI result at the trip wire location. The agreement with the higher Re_c data is better. XFOIL does remarkably well in predicting the C_p distribution.

Figure 7(b) compares the skin friction coefficient (C_f) distribution over the airfoil surface between FDL3DI prediction, XFOIL prediction, and measured data from Sagrado *et al* [43]. Excellent agreement is seen between the FDL3DI predictions and the measured data. Large differences between XFOIL and FDL3DI are observed near the trip wire location ($x/c = 0.05$) as expected. In FDL3DI, the trip wire triggers an instability wave that induces transition over a finite distance, while in XFOIL the transition appears

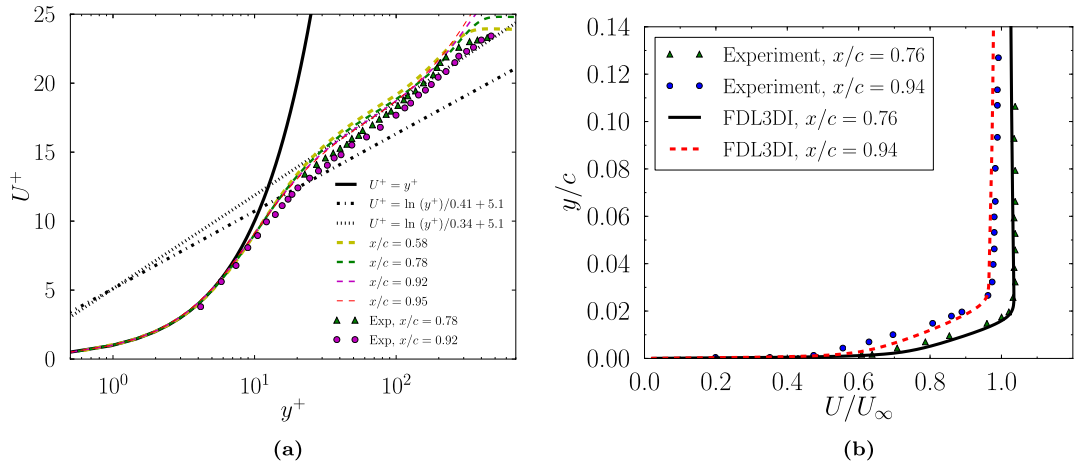

Figure 9. Baseline time- and span-averaged velocity profile comparisons of the current LES predictions and experiment from (a) Lee and Kang [46] and (b) Sagrado *et al* [43]. (a) Velocity profile in wall units. (b) Velocity profile in physical scale.

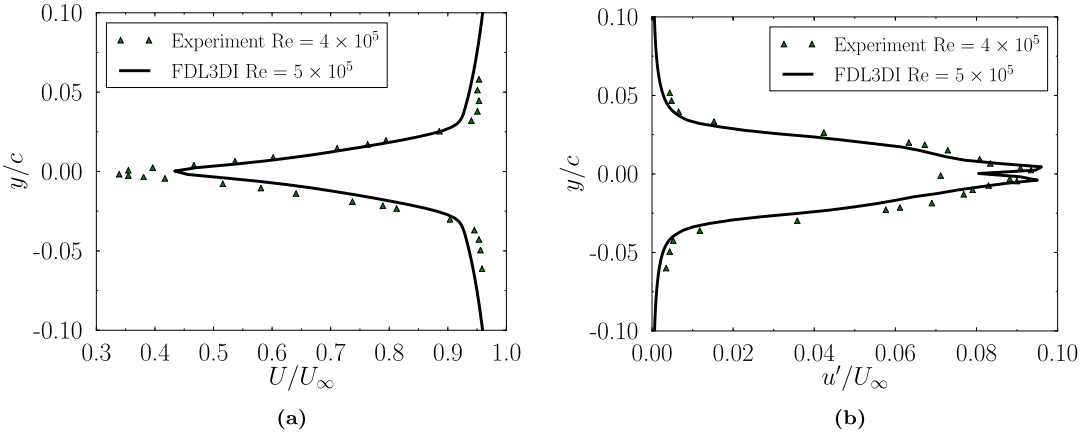

Figure 10. Baseline time- and span-averaged velocity and turbulence intensity comparisons of the simulation and experiment from Sagrado *et al* [43] at $x/c = 1.02$. (a) Velocity. (b) Turbulence intensity.

to occur immediately. Despite this difference, the two predictions agree reasonably well in the aft portion of the airfoil where the boundary layer is turbulent in both the simulations.

Figure 8 shows the span-averaged surface pressure spectrum (Φ) for the baseline airfoil at $x/c = 0.98$. The spectrum is normalized by the inner variables as $\Phi(\omega)/(\tau_w^2\nu/u_\tau^2)$, where τ_w is the wall shear stress, ν is the kinematic viscosity, u_τ is the friction velocity and ω is the angular frequency. The predicted spectra were computed using 1400 samples spanning over $2.5\,\tau$ of simulation data. The wall pressure spectrum is expected to follow a power-law behavior, $\Phi(\omega) \sim \omega^n$, where the exponent n is dependent on the frequency range of the turbulent spectrum. The ω^{-5} behavior is associated with sources in the boundary layer below y^+ of 20 [45]. Figure 8 shows that the predicted turbulent spectrum follows the expected power-law behavior. Measurements of surface pressure spectra at multiple chordwise locations are available in figure 13(b) of [43] (not reproduced here); the measurements are for a NACA 0012 airfoil at $AOA = 0°$ and $Re = 2 \times 10^5$ and 4×10^5. There is good agreement between the current LES results and the measurements in terms of the frequency range over which the wall pressure spectra follow the ω^{-5} behavior.

Figure 9(a) compares the baseline time- and span-averaged normalized velocity (U^+) profiles at different chordwise locations on the aft portion of the airfoil. The profiles follow the expected $U^+ = y^+$ trend in the viscous sublayer. The slope in the log-law region is found to be $1/0.34$ in the simulations and in the measurements reported in [46]. This slope is slightly different than the value of $1/0.41$ obtained with the von Kármán constant. Nagib *et al* [47] found that the von Kármán constant is not universal and is dependent on the flow geometry and pressure gradient. Experiments by Lee and Kang [46] for turbulent flow over a NACA 0012 airfoil at $Re_c = 600\,000$ found the slope to be closer to $1/0.34$ (see figure 9(a)).

Figure 9(b) compares the current LES predictions of the time- and span-averaged velocity profiles, U/U_∞ for the baseline airfoil with the measurements from Sagrado *et al* [43]. The agreement is good except very near the airfoil surface where the velocity is slightly lower in the measurements. Similar differences

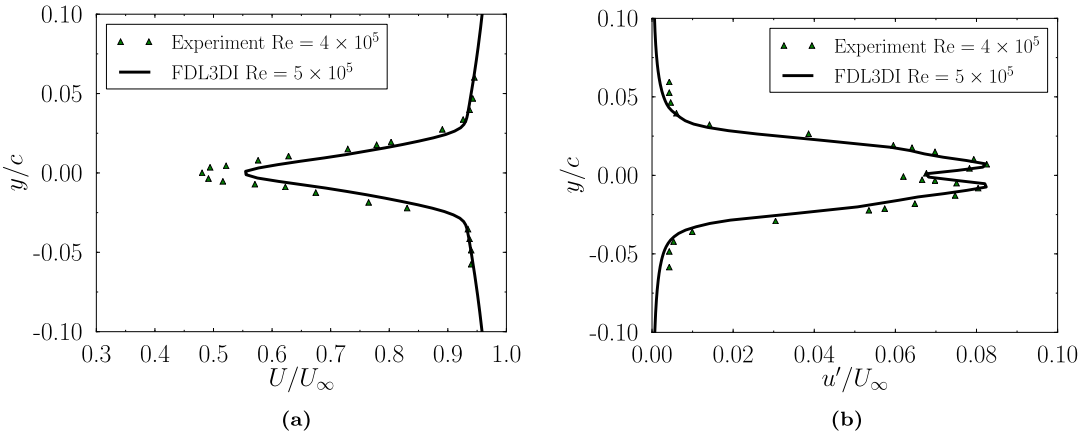

Figure 11. Baseline time- and span-averaged velocity and turbulence intensity comparisons of the simulation and experiment from Sagrado *et al* [43] at $x/c = 1.05$. (a) Velocity. (b) Turbulence intensity.

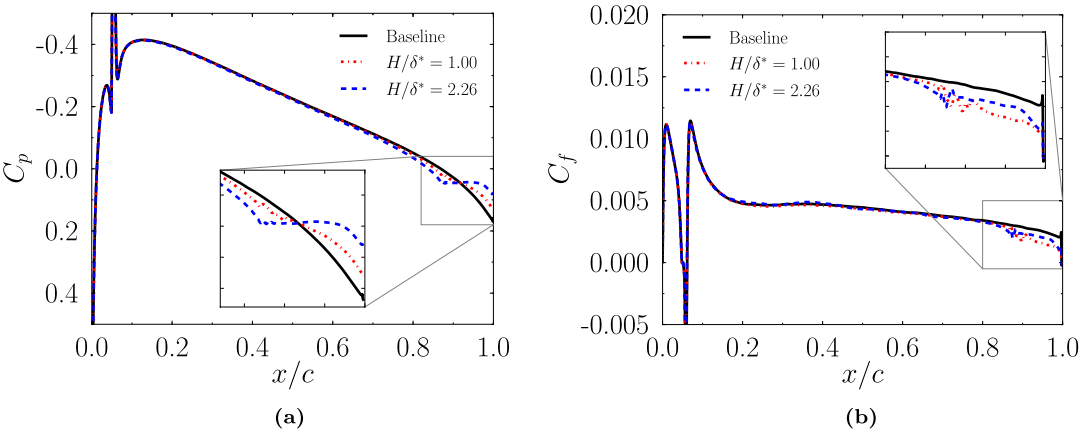

Figure 12. Time- and span-averaged C_p and C_f distributions compared between the baseline and the two fence simulations. (a) C_p. (b) C_f.

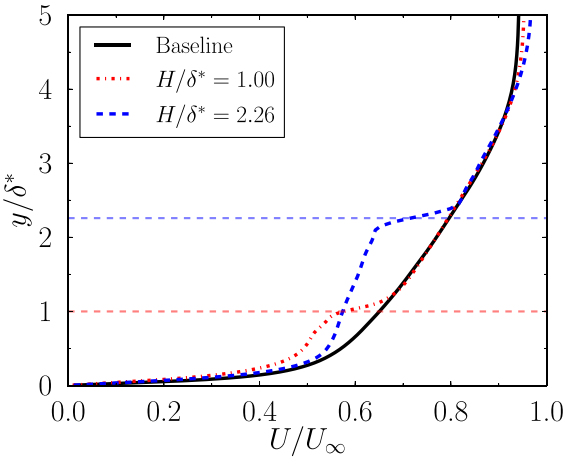

Figure 13. Predicted wall-normal velocity profiles at $x/c = 0.975$. The profiles are averaged over the span. The horizontal dashed lines represent the top of the fences.

have been observed in other LES predictions (see e.g. Wolf and Lele [48]).

Figures 10 and 11 compare the predicted time- and span-averaged velocity and turbulence intensity profiles at two locations in the airfoil wake with measurements from Sagrado *et al* [43]. The agreement is generally good except the peak wake deficit at $y/c = 0.0$ is slightly underpredicted. Correspondingly, the turbulence intensity at that location is slightly over predicted in the LES results. As with the velocity profiles, similar

Table 2. Drag coefficient (C_D) comparisons between the baseline and fence simulations.

Geometry	C_D	C_D % increase	Wetted area %increase
Baseline	0.012 12	—	—
$H/\delta^* = 1.0$	0.012 53	3.36	9.47
$H/\delta^* = 2.26$	0.013 72	13.2	22.1
$H/\delta^* = 1.0$ (neglecting lateral/front fence sides)	0.012 02	−0.81	0.0
$H/\delta^* = 2.26$ (neglecting lateral/front fence sides)	0.012 01	−0.90	0.0

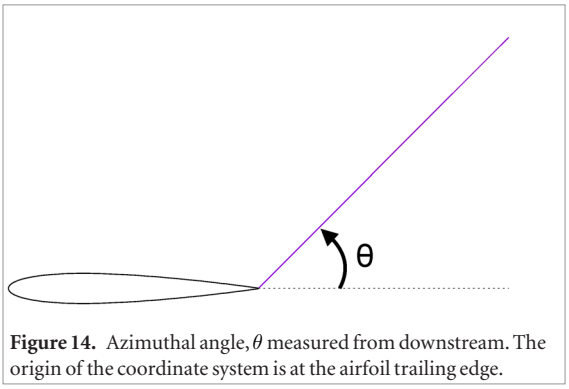

Figure 14. Azimuthal angle, θ measured from downstream. The origin of the coordinate system is at the airfoil trailing edge.

differences were observed in the LES predictions by Wolf and Lele [48].

4.2. Aerodynamic performance

Figure 12 compares the time- and span-averaged C_p and C_f distributions over the airfoil surface between the baseline and the two fence geometries. In this and other plots that show span-averaged results, unless specified otherwise, the points that lie on and within the fence walls are removed in the averaging procedure for the fence simulations. Outside of the fence region, the C_p and C_f distributions are nearly identical for the three simulations. For the fences, both C_p and C_f drop below the corresponding baseline values in the fence region.

Figure 13 shows the time- and span-averaged wall-normal velocity in the fence region at $x/c = 0.975$. From the airfoil surface to the top of the fences (shown by horizontal dashed lines), there is a lower velocity gradient with the fences than with the baseline. Above the fence height, the velocity abruptly changes for both fences while the velocity gradient of the baseline remains smooth. This sudden inflection in velocity profile is typical of canopy flows [25]. The reduced gradient near the wall is responsible for the reduced wall skin friction seen earlier in figure 12(b).

Since the fences maintain the flow symmetry for the AOA $= 0°$ case investigated, the mean lift ($=0$) is unaffected by the fences. The drag coefficient ($C_D = D/(q_\infty S.c)$) of the baseline and fence geometries is compared in table 2. Here $q_\infty = \frac{1}{2}\rho_\infty u_\infty^2$, S is airfoil span, and c is airfoil chord. Note that the surface area ($=S \times c$) used to compute C_D is unchanged between baseline and fences.

In the first three rows of table 2, C_D is computed by integrating the x component of the forces acting on the airfoil surface and the side-, front-, and top walls of the fences. The drag for both fences is larger than the baseline although the percentage increase is small, particularly with the smaller fence. Note that the increase in C_D is substantially smaller than the increase in the wetted surface area (additional surface area due to the fence side and front walls). To further analyze this, C_D is also computed by *ignoring* the contribution from the side and front walls of the fences; the contribution from the top wall is still included. These values are listed in the last two rows of table 2. When computed this way, the C_D is slightly lower for the fences compared to the baseline due to the reduction in C_f within the fence channels (see figure 12(b)). Furthermore, there is virtually no difference in C_D between the two fence heights.

The net aerodynamic effect of the fences is an increase in drag with the percentage increase equal to 3.36 and 13.2 respectively for the short and tall fences.

4.3. Aeroacoustic performance

The in-house Ffowcs Williams–Hawkings (FW-H) solver described in section 2.2 is used to calculate the far field noise. A porous integration (Kirchoff) surface is used that is approximately half chord away from the airfoil surface. Data is sampled for approximately four characteristic times (4τ) for a total of 1200 samples. The data is segmented into 13 intervals for spectral averaging using Welch's method [49].

Figure 15 plots the predicted far field noise spectra for the baseline and the two fences at the azimuth angle, $\theta = 90°$. The azimuth angle is measured from downstream, and is positive in the counter-clockwise direction (see figure 14). The origin of the coordinate system is at the airfoil trailing edge ($x = c$, $y = 0$). The observer location is at $x = c$, $y = 12c$ and mid-span. The dimensional frequencies in figure 15, and in the remainder of the text are obtained by scaling the non-dimensional simulation results to the experimental conditions. The reference length and velocity scales in the experiment [26] are: airfoil chord length of 0.8 m and free stream velocity of 50 m s^{-1}.

As seen in figure 15, a large reduction in the farfield SPL is observed with both fences for frequencies (f) greater than 1.5 kHz. Between 600 Hz–1.5 kHz, noise reduction is observed only with the shorter fence. In contrast, for $f > 2$ kHz, the taller fence is quieter than the shorter fence. Figure 16 plots the measured [26] farfield spectra for a different baseline airfoil (DU96-W-180) and two fence geometries, and is shown here for a qualitative comparison with the prediction results plotted in figure 15. The measured farfield noise was obtained using acoustic beamforming over a two-dimensional area near the trailing edge. The data in figure 16 is for the $-0.5°$ angle-of-attack case for the DU96-W-180 airfoil. In the experiment [26], the maximum heights of the two fences were 4 and 8

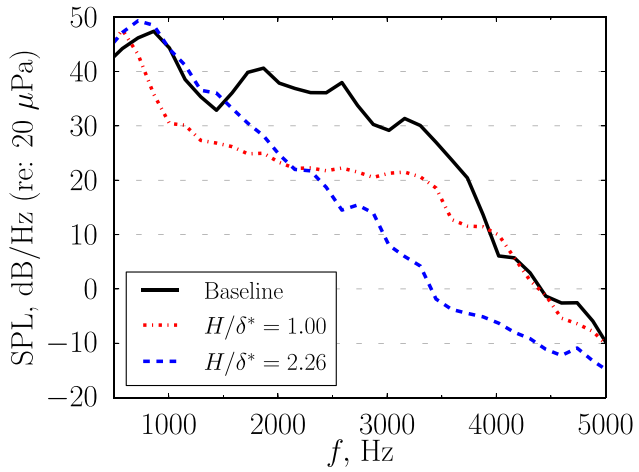

Figure 15. Predicted farfield noise spectra at an observer located at $\theta = 90°$.

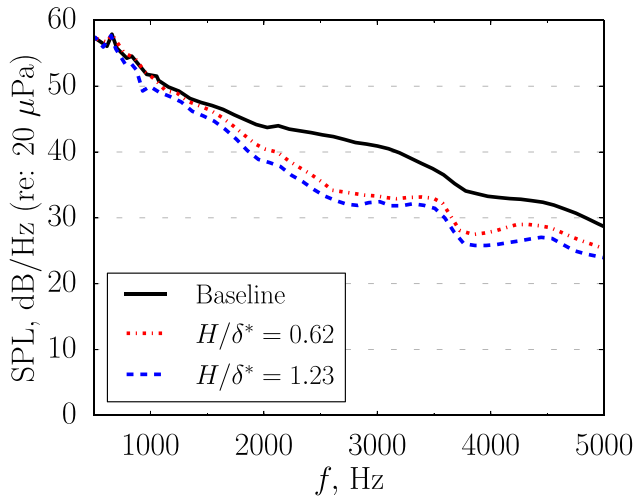

Figure 16. Measured farfield sound spectra from Clark *et al* [26]. The nondimensional fence pitch, $P/\delta^* = 0.69$ in the experiment.

mm. An estimate of δ^* for the DU96-W-180 for this case is obtained using XFOIL, and the scaled maximum heights of the two fences, H/δ^* are found to be 0.62 and 1.23 on the suction side and 0.98 and 1.96 on the pressure side. The estimates from XFOIL were obtained by forcing the flow to transition at the same location that the trip wire was placed in the experiment, which was at $x/c = 0.05$ and $x/c = 0.10$ on the suction and pressure surface, respectively. Note that the value of the displacement thickness slightly varies depending on the location of the trip.

Kato's correction [37] is used to account for the difference in the simulated span and the span over which the measured data is integrated during Beamforming in the measurement of farfield sound. The general trend of larger noise reduction (for $f > 2$ kHz) with taller fences is the same as the experimental observation even though the reduction is much greater in the simulations. For $f < 2$ kHz, the simulations predict the taller fence to be louder than the shorter fence but the experiments found the taller fence to be quieter over the entire spectrum. The experiment data shows no measurable difference between the baseline and the two fence geometries at these low frequencies. Clark *et al* [26] noted that the measurements may be limited by the facility noise for $f < 1$ kHz; hence any potential noise reduction at those frequencies is not captured by the measurements.

The following differences between the experiment and the simulations can explain the differences in the predicted and measured trends: (1) The baseline airfoils are different; the simulations are for a symmetric (NACA 0012) airfoil while the measurements use the asymmetric DU96-W-180 airfoil, (2) the scaled fence heights, H/δ^* are substantially different; while the taller fence in the simulations has $H/\delta^* = 2.26$, the taller fence in the experiment has $H/\delta^* = 1.23$, and (3) the scaled pitch of the fences, P/δ^* in the simulations is 1.49, which is approximately double of that in the experiment ($= 0.69$).

Figure 17 shows the predicted farfield noise spectra at two observer locations at azimuth angles of $\theta = 45°$ and 135°. The trends for the noise reduction are the same as with $\theta = 90°$, i.e. noise reduction

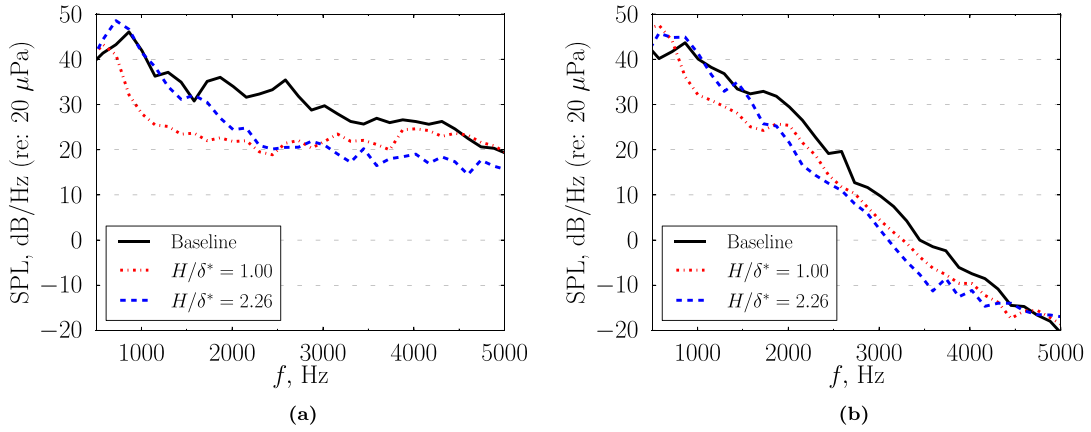

Figure 17. Predicted farfield noise spectra at observer locations: (a) $\theta = 45°$ and (b) $\theta = 135°$.

is observed with only the shorter fence for $f < 1.5$ kHz but with both fences for $f > 1.5$ kHz, where a greater noise reduction is observed with the taller fence for $f > 2$ kHz. Although the trend of noise reduction is similar to $\theta = 90°$, the *SPL* difference between the fences and the noise reduction compared to the baseline are smaller, especially at $f > 2$ kHz.

To quantify the overall noise reductions, band sound pressure level (L_{pb}), defined as

$$L_{pb} = 10 \log_{10} \sum_{f_{\min}}^{f_{\max}} \left(|\hat{p}(f_i)|/p_{\text{ref}}\right)^2, \qquad (5)$$

is computed, where $p_{\text{ref}} = 20$ μPa, and $f_{\min}$ and $f_{\max}$ correspond to the minimum and maximum frequencies of the band level over which the spectra is integrated. We integrate over different frequency ranges to quantify the variation of noise reduction with frequency.

The difference in computed band pressure level, ΔL_{pb} between the baseline and the two fence geometries for azimuth angle $\theta = 90°$ are listed in table 3. As seen in the first column, integrating over the entire frequency range results in a L_{pb} reduction of 5.43 dB with the short fence ($H/\delta^* = 1.0$). However, with the taller fence ($H/\delta^* = 2.26$), the L_{pb} increases slightly ($\approx$ 0.54 dB). The second column, which is obtained by integrating over the low frequencies (500 Hz–2 kHz), shows a L_{pb} reduction of 4.86 dB with the shorter fence and an increase of 1.2 dB with the taller fence. Integrating over only the high frequencies (2–5 kHz), as shown in the third column, a significant reduction in L_{pb} is seen with both fences, where a larger reduction is observed with the taller fence. The results of the integrated band pressure level for azimuth angles $\theta = 45°$ and 135° are shown in tables 4 and 5. The trends for noise reduction are the same as with $\theta = 90°$, except with smaller noise reductions in the 2–5 kHz frequency range.

To estimate the reduction in radiated sound power, the L_{pb} is integrated over all azimuth angles and the results are listed in table 6. The trends for the noise reduction are the same as seen in tables 3–5, which shows that the total sound power generated is reduced at the source.

4.4. Noise reduction mechanisms

Two hypotheses are put forth to explain the observed farfield noise reduction with the finlet fences:

1. The fences lift the turbulence eddies away from the scattering (airfoil trailing) edge, and
2. the fences reduce the spanwise correlation length.

These hypotheses are investigated using the simulation results in this section.

4.4.1. Turbulence kinetic energy

To assess the first hypothesis, the normalized turbulence kinetic energy (TKE) is obtained by averaging the time-accurate flow data over 2.6τ; the TKE field did not change significantly with doubling the sampling duration. Contour plots of normalized TKE at $x/c = 0.975$ are compared between the baseline and fence simulations in figure 18. This is the chordwise location where the fences reach the maximum height. It is clear from the figure that for both fences, the TKE reduces near the airfoil surface and increases above the fences.

The time-averaged data is further averaged along the span and the span-averaged profiles are compared in figure 19. In the figure, the vertical axis is the wall-normal distance normalized by δ^*, and the horizontal dashed lines represent the location of the top of the fences. The profiles show a significant reduction in TKE near the airfoil surface due to the fences; furthermore, the reduction is greater with the taller fence. The location of peak TKE is symptomatic of the location of the noise source (the fluctuations in the turbulence). Note that direct radiation from this source is not as efficient as indirect radiation due to scattering of the hydrodynamic field of this source by the airfoil trailing edge. Figure 19 therefore verifies the first

Table 3. Difference in L_{pb} between baseline and fences at $\theta = 90°$.

Geometry, H/δ^*	ΔL_{pb}, dB 500 Hz–5 kHz	ΔL_{pb}, dB 500 Hz–2 kHz	ΔL_{pb}, dB 2 kHz–5 kHz
1.0	−5.43	−4.86	−12.89
2.26	0.54	1.20	−16.74

Table 4. Difference in L_{pb} between baseline and fences at $\theta = 45°$.

Geometry, H/δ^*	ΔL_{pb}, dB 500 Hz–5 kHz	ΔL_{pb}, dB 500 Hz–2 kHz	ΔL_{pb}, dB 2 kHz–5 kHz
1.0	−6.08	−5.93	−7.09
2.26	1.14	1.77	−9.54

Table 5. Difference in L_{pb} between baseline and fences at $\theta = 135°$.

Geometry, H/δ^*	ΔL_{pb}, dB 500 Hz–5 kHz	ΔL_{pb}, dB 500 Hz–2 kHz	ΔL_{pb}, dB 2 kHz–5 kHz
1.0	−0.59	−0.54	−4.57
2.26	1.54	1.61	−8.42

Table 6. Difference in L_{pb} between baseline and fences after integrating over all azimuth angles.

Geometry, H/δ^*	ΔL_{pb}, dB 500 Hz–5 kHz	ΔL_{pb}, dB 500 Hz–2 kHz	ΔL_{pb}, dB 2 kHz–5 kHz
1.0	−3.62	−3.21	−8.77
2.26	1.09	1.63	−11.14

hypothesis: fence finlets indeed increase the separation distance between the source and the airfoil trailing (scattering) edge.

The increased source separation from the airfoil trailing edge leads to inefficient scattering (noise radiation), which is explained below. Ffowcs Williams and Hall [3] studied how turbulent eddies scatter from the edge of a half plane. Edge scattering is most intense when an eddy is well within an acoustic wavelength of the edge, i.e. $2kr_o \ll 1$, where k is the acoustic wave number, and r_o is the distance from the center of the eddy to the edge. When this condition is met, the intensity of the scattered sound, $I \propto \alpha^2/r_o^3$, where α is the normalized turbulence intensity [3]. When the eddies are far enough from the edge ($\sqrt{kr_o} \gg 1$), then the eddies radiate as if in free space and the edge does not produce any significant sound amplification. Therefore, as the turbulence intensity reduces or the peak turbulence shifts away from the edge, the intensity of the sound emitted from the edge should decrease.

The predicted TKE profiles are examined against measured turbulence intensity (TI) profiles reported in Afshari *et al* [50]. A different experiment is selected for this comparison as Clark *et al* [26] did not report velocity measurements. Afshari *et al* [50] investigated the effect of finlets installed in the turbulent boundary layer over a flat plate. Figure 20 plots profiles of rms of the fluctuating streamwise flow velocity, u_{rms} normalized by the freestream velocity, U_∞. In terms of the baseline δ^* at $x/c = 0.975$, the fences in the experiment had maximum heights $H/\delta^* = 0.98$ and 1.46, and pitch $P/\delta^* = 0.30$. It should be noted that these velocity measurements were taken downstream of the fences instead of between the fences as is done in the current predictions; the fences in the experiment were placed at $x/c = 0.64$ to $x/c = 0.82$ and velocity measurements taken at $x/c = 0.975$. Despite these differences, the trend in the current predictions (see figure 19) is consistent with the measurements, i.e. the turbulent fluctuations (represented by u_{rms} and TKE) decrease near the flat plate/airfoil surface and increase above the fences. Also, in both the experiment and simulation, increasing the fence height results in lesser turbulent fluctuations near the surface.

4.4.2. *Surface pressure spectra*

The primary noise generation mechanism for low Mach number flow over an airfoil is trailing edge noise. The hydrodynamic energy in the boundary layer turbulence results in unsteady surface pressure, primarily near the edge, which radiates as an unsteady lift (dipole) source. Unsteady surface pressure near the trailing edge is therefore a measure of the strength of the noise source. Surface pressure spectra are computed at $x/c = 0.975$. Numerical data is collected for approximately $6\,\tau$. Welch's method [49] is used with 1655 samples divided into 20 segments to reduce the scatter in the spectra by spectral averaging. The spectra are further averaged along the span to obtain an overall measure of reduction in spectral magnitude with the fences. The grid planes (ζ = constant) that have grid points inside the fence region, which are not solved by FDL3DI, are removed in the averaging procedure.

Figure 21(a) compares the predicted surface pressure spectra from the baseline and the two fence simulations. Compared to the baseline, a measurable reduction at high frequencies ($f > 2$ kHz) and a small increase at low frequencies is observed in the predicted spectra for the $H/\delta^* = 1.0$ fence geometry. The taller fence exhibits a similar trend except a greater reduction in the surface pressure spectra is observed at all frequencies. The crossover frequency, at which the surface pressure spectra switches from being higher than baseline to lower than the baseline, is smaller with the larger fence.

These observations are compared with the measured surface pressure spectra from Clark *et al* [51] in figure 21. In the experiment [51], unsteady surface pressure data was only measured with the baseline airfoil and the $H/\delta^* = 1.23$ fence. The predictions agree

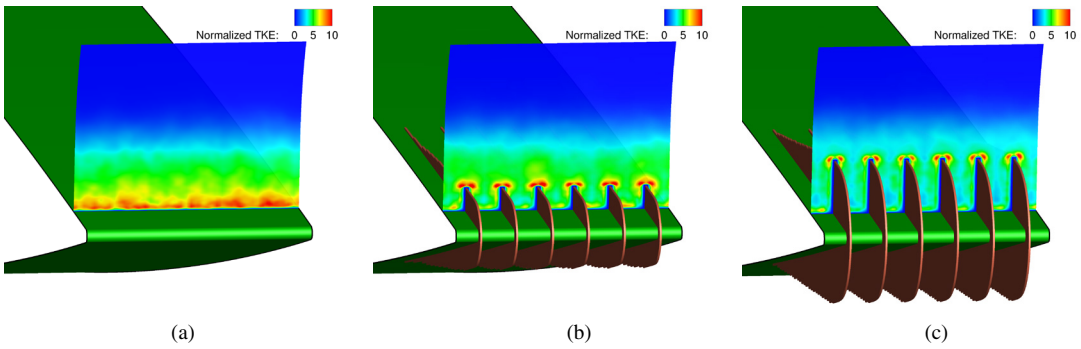

Figure 18. Normalized turbulent kinetic energy, $\mathrm{TKE}/{u_\tau}^2$ at $x/c = 0.975$ for (a) baseline, (b) $H/\delta^* = 1.0$ fence, and (c) $H/\delta^* = 2.26$ fence.

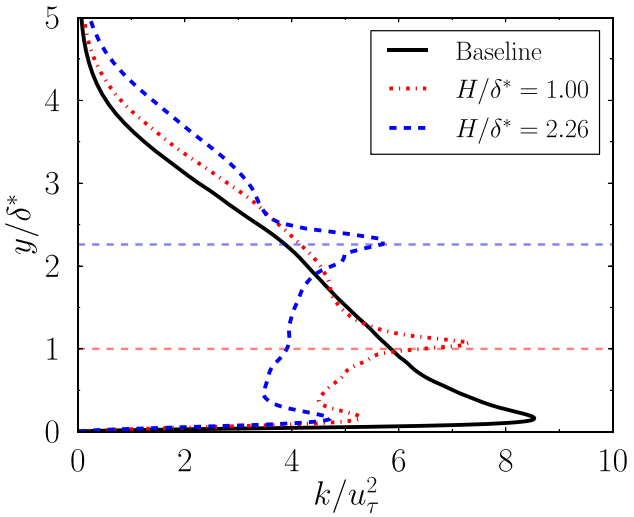

Figure 19. Predicted normalized turbulent kinetic energy, $\mathrm{TKE}/{u_\tau}^2$ profiles at $x/c = 0.975$. The profiles are averaged over the span. The horizontal dashed lines represent the location of the top of the fences.

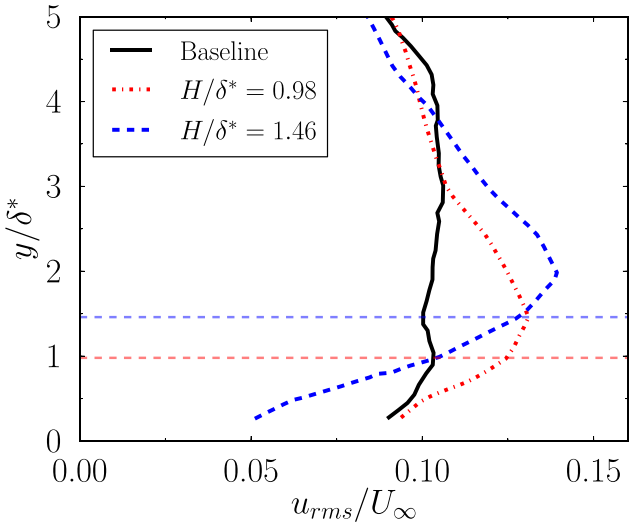

Figure 20. Measured profiles of $u_{\mathrm{rms}}/U_\infty$ from the flat plate experiment by Afshari *et al* [50]. The profiles are measured downstream of the fences. The horizontal dashed lines represent the maximum height of the fences.

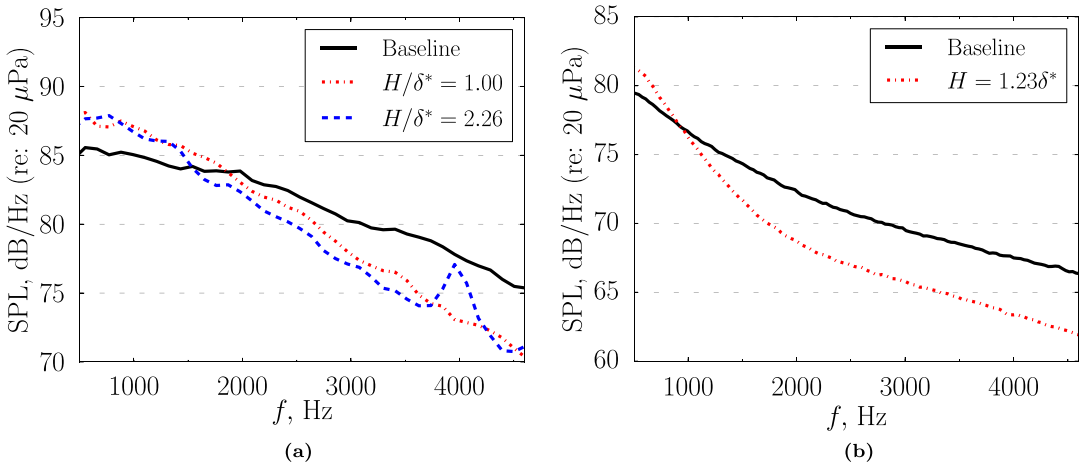

Figure 21. Qualitative comparison between the predicted and measured surface pressure spectra near the airfoil trailing edge ($x/c = 0.975$). Measured data is from Clark *et al* [51] with a scaled fence pitch $P/\delta^* = 0.77$. (a) FDL3DI predicted surface pressure spectra. (b) Measured surface pressure spectra.

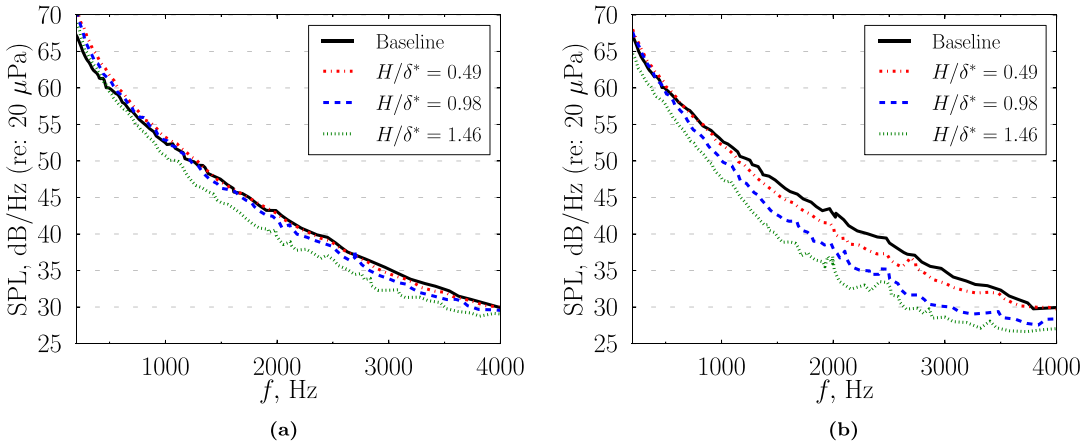

Figure 22. Measured surface pressure spectra from Afshari *et al* [50]. The profiles are measured downstream of the fences. Measurements are for a nondimensional fence pitch, $P/\delta^* =$ (a) 0.30 and (b) 1.03.

qualitatively with the measurements with reduction in spectral magnitude observed at high frequencies and an increase at low frequencies. However, the crossover frequency is lower in the measurements.

A broad peak is observed around 4 kHz in the predicted spectrum for the taller fence. Spectra were obtained at various chordwise locations and it was found that the peak is maximum at x/c where the maximum fence height occurs. Resonance in the channels between adjacent fences (cascade resonance) could explain the presence of this peak.

Afshari *et al* [50] assessed the effect of fence height on unsteady surface pressure for two fence spacings ($P/\delta^* = 0.30$ and 1.03) in their flat-plate experiment. The measured spectra are plotted in figure 22. The measurements show the same trends as in the predictions (compare with figure 21): (1) increasing the fence height results in further reductions in the unsteady surface pressure at the trailing edge; reductions are limited to high frequencies, and (2) the crossover frequency reduces with increasing fence height.

4.4.3. *Velocity spectra*

The span-averaged velocity power spectral density (PSD) of the vertical and horizontal velocity fluctuations in the viscous sublayer ($y/\delta^* = 0.045$) at $x/c = 0.975$ are shown in figure 23. There is a reduction observed in the vertical velocity fluctuations with both fences compared to the baseline particularly at high frequencies. Greater reduction is observed with the taller fence. The same trend is observed in the horizontal velocity fluctuations. Afshari *et al* [50] reported the velocity PSD measured at $x/c = 0.975$ for fence heights, $H/\delta^* = 0.49, 0.98$, and 1.46 with a fixed pitch, $P/\delta^* = 0.30$. The contour plots near the flat plate surface (see [50]) showed the same behavior as is seen in the current predictions, i.e. greater reductions are observed with the taller fences and at high frequencies.

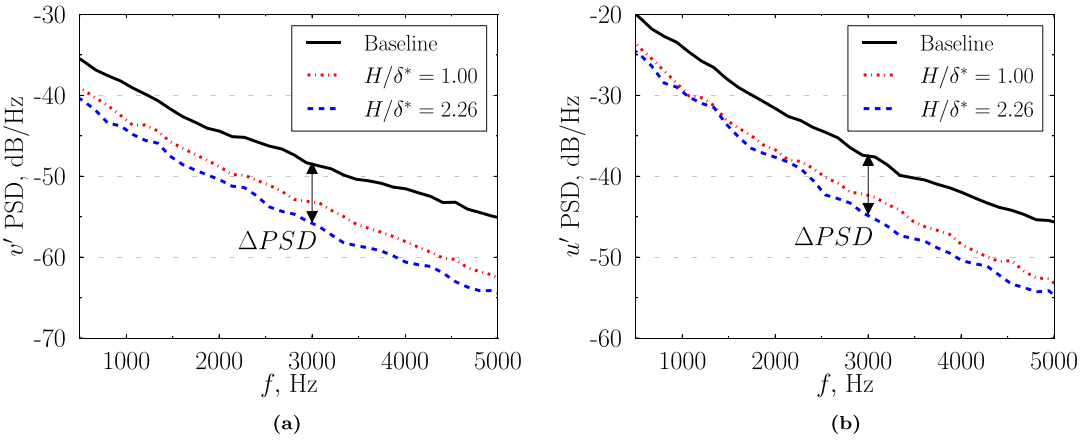

Figure 23. FDL3DI predicted velocity fluctuation spectra in the (a) vertical and (b) horizontal directions within the viscous sublayer ($y/\delta^* = 0.045$) at the trailing edge $x/c = 0.975$. Predictions are averaged along the span with the points within the fences removed from the averaging procedure. (a) Vertical velocity fluctuations spectra. (b) Horizontal velocity fluctuations spectra.

4.4.4. *Review of the first hypothesis*

The observations are summarized here. For $f > 2$ kHz, the farfield noise reduces with both fences, with higher reductions observed for the taller fence. Commensurate with the farfield noise reductions, the near-surface velocity fluctuations and the unsteady surface pressure reduce with the fences for $f > 2$ kHz, and larger reductions are seen with the taller fence. In addition, it is shown that with the fences, the TKE reduces near the surface and increases above the fences; higher TKE reduction is observed with the taller fence. These results substantiate the first hypothesis to explain the measured farfield noise reductions: the fences lift the turbulence eddies away from the scattering (trailing) edge thereby increasing the distance between the noise source (turbulence) and the airfoil trailing edge. Because of the increased source-scattering edge separation distance, the high frequency ($f > 2$ kHz) surface pressure fluctuations reduce, which reduces the scattering efficiency of the trailing edge, leading to farfield noise reduction. Increasing the fence height increases the source-scattering edge separation distance which further reduces the unsteady surface pressure and the farfield sound.

4.4.5. *Spanwise coherence*

Next we study spanwise coherence to investigate the second hypothesis. Dependence of farfield noise on spanwise coherence can be assessed using Amiet's theory [4] which gives an analytical expression of the farfield pressure PSD, $S_{pp}(\omega)$ of sound radiated from a turbulent flow past the trailing edge of a half-plane. Per Amiet [4], $S_{pp}(\omega) \propto l_y(\omega) S_{qq}(\omega)$, where ω is the angular frequency, $l_y(\omega)$ is the spanwise correlation length of the pressure fluctuations, and $S_{qq}(\omega)$ is the surface pressure PSD. A reduction in spanwise coherence (a measure of $l_y(\omega)$) can cause farfield noise reduction even if the surface pressure PSD remains unchanged.

Coherence squared (γ^2) between two points $\mathbf{x}$ and $\mathbf{y}$ is defined as

$$\gamma^2_{xy}(\omega) = \frac{|S_{xy}(\omega)|^2}{S_{xx}(\omega) S_{yy}(\omega)}, \tag{6}$$

where $S_{xx}(\omega)$ is the power spectral density (PSD) evaluated at $\mathbf{x}$ and $S_{yy}(w)$ is the PSD at $\mathbf{y}$. For spanwise coherence, points $\mathbf{x}$ and $\mathbf{y}$ are at a given chordwise location (x/c) but separated in the span direction such that $\mathbf{y} = \mathbf{x} + \Delta z\, \hat{e}_k$, where $\hat{e}_k$ is a unit vector along the span direciton. The reference location to compute spanwise coherence is varied along the span. Each grid point is selected as a reference to compute one instance of coherence. All the instances of coherence so computed (101 in total) are then averaged to obtain the γ^2 reported here.

Equation 6 is used with the aforementioned span averaging to compute $\gamma^2_{xy}(\omega)$ for the baseline and fence simulations. A total of $6\,\tau$ of data, consisting of 1655 samples divided into 20 segments for spectral averaging is used for the calculations. Figure 24 compares γ^2 of the unsteady surface pressure near the trailing edge ($x/c = 0.975$) as a function of the spanwise separation distance ($\Delta z/c$) for the baseline and fence simulations. Coherence plots are drawn for two example frequencies to highlight the characteristics in the low- and high-frequency regions. The vertical dashed lines in the plots represent the spanwise location of the fences. The fences are equidistant and the pitch is P.

Focusing on γ^2 for separation distances greater than the fence pitch, i.e. $\Delta z/c > P/c$, we note that the fences reduce γ^2 at low frequencies; a larger reduction in γ^2 is obtained with the taller fence. At high frequencies, the coherence is already small for $\Delta z/c > P/c$ and the fences do not reduce it any further. The simulation results show a farfield noise reduction at low frequencies (see figure 15) with the $H/\delta^* = 1.0$ fence despite an increase in the unsteady surface pressure PSD (see figure 21(a)). This analysis suggests that the

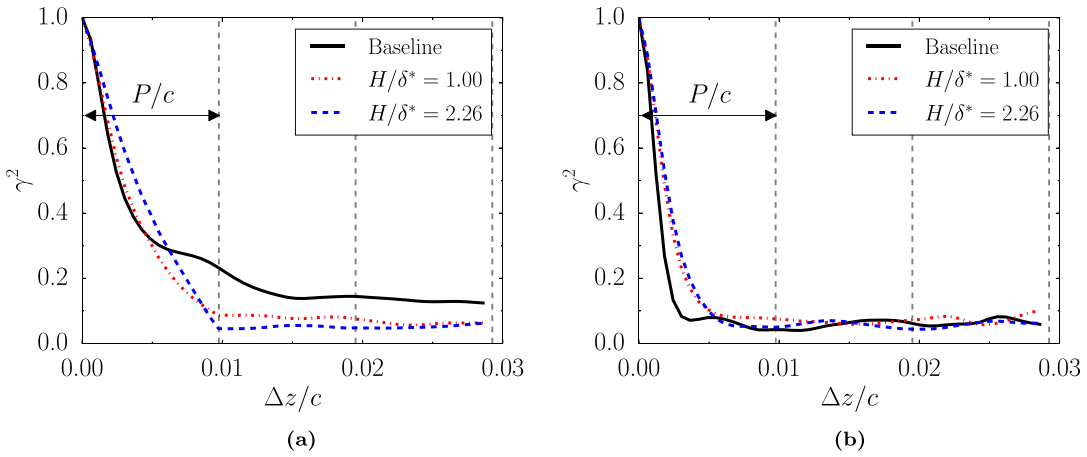

Figure 24. Spanwise coherence, $\gamma^2(\omega)$ of unsteady surface pressure at the trailing edge $x/c = 0.975$ for (a) low, and (b) high frequencies. (a) Low frequency, $f = 550$ Hz. (b) High frequency, $f = 3000$ Hz.

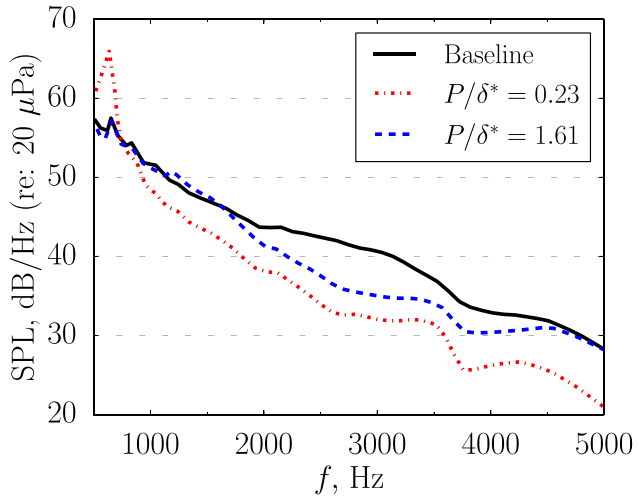

Figure 25. Measured farfield noise spectra from Clark *et al* [26] showing the effect of fence spacing. For all cases, the normalized maximum height of the fences, $H/\delta^* = 0.62$ on the suction side.

reduction in spanwise coherence at low frequencies is responsible for the reduction in farfield noise.

This argument is supported by the following observation of the results from Clark [26]. Low-frequency noise reduction is observed when the fence pitch is reduced (see figure 25). Since fences successfully reduce γ^2 for spanwise distances greater than a fence pitch, a tighter pitch implies a reduction in span correlation length, and hence farfield noise.

For a separation distance smaller than the fence pitch, i.e. $\Delta z/c < P/c$, γ^2 increases due to the fences. This is observed for both fences at high frequencies, but only for the taller fence at low frequencies. Adjacent fences act as channel walls bounding the flow, thereby increasing the coherence within each channel/passage. The taller fences create a stronger 'channeling' effect and it correspondingly has a greater increase in γ^2. At high frequencies (small wavelength), the increase in source-trailing edge separation dominates over the increase in γ^2 and farfield noise reduction is observed

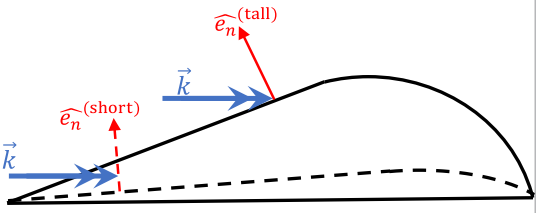

Figure 26. A schematic illustrating the effect of increasing the maximum fence height on the angle between the oncoming boundary layer turbulence wavenumber vector ($\vec{k}$) and the fence normal ($\hat{e_n}$). Highest sound radiation from the fence edge would occur when $\vec{k}$ and $\hat{e_n}$ are parallel.

with fences. At low frequencies the increase in source separation distance is small (corresponding to the acoustic wavelength) with the fences and hence the spanwise coherence becomes a dominant factor. This increase in γ^2 within fence passages would therefore imply an increase in the radiated farfield sound with

the taller fence in comparison to the smaller fence, which is indeed observed in the numerical predictions (see figure 15).

Another potential reason for the taller fence to be louder than the shorter fence at low frequencies, even though the taller fence has lower pressure PSD on the airfoil surface (see figure 21), is the additional noise due to scattering from the leading edge of the fence. As the maximum fence height increases, the leading edge of the fence becomes less aligned with the flow (see figure 26), increasing the energy in the wavenumber component (of the boundary layer turbulence) normal to the fence edge. This results in an unsteady force on the fence leading edge which radiates noise as a dipole source. The noise generation mechanism is the same as for the leading edge noise problem investigated in Amiet [52].

5. Conclusions

This paper presents numerical investigations of airfoil geometries inspired by the down coat of the owl. The down coat is modeled using finlet fences proposed by Clark *et al* [24]. Large eddy simulations are performed for the zero-lift case (AOA = 0 degree) for the baseline (NACA 0012) airfoil and two airfoils with fences attached to the aft portion of the airfoil. Two fences with different maximum nondimensional heights, $H/\delta^* = 1.0$ and 2.26, are investigated.

The aerodynamic analysis shows that the drag increase due to the fences is small and is due to the increased wetted surface area. The skin friction coefficient on the airfoil surface reduces because of fences and hence the drag increase is smaller than the increase in the wetted surface area.

An in-house FW-H solver is used with the LES data to predict the farfield noise and evaluate the aeroacoustic performance of the fences. Compared to the baseline, the $H/\delta^* = 1.0$ fence reduces the farfield SPL by up to 10 dB for frequencies between 500 Hz and 5 kHz. Noise reduction with the taller fence ($H/\delta^* = 2.26$) is limited to frequencies above 1.5 kHz. Larger noise reduction is observed with the taller fence for frequencies greater than 2 kHz.

Two noise reduction mechanisms are identified: (1) the fences increase the source-scattering edge separation distance rendering the scattering process inefficient, particularly for high-frequency noise, and (2) the fences reduce the spanwise coherence (γ^2) in the boundary layer for separation distances greater than the fence pitch, which is more effective at reducing low-frequency farfield noise.

The first mechanism of noise reduction is verified by examining the TKE near the airfoil trailing edge and the unsteady surface pressure spectra. The fences reduce the TKE near the airfoil (scattering) surface; peak TKE shifts to just above the fence height. The reduced TKE near the surface leads to reduced unsteady surface pressure, which is observed in the simulations and previous measurements. The taller fence gives greater reductions in near-surface TKE, surface pressure PSD, and farfield noise for frequencies greater than 2 kHz.

Spanwise coherence of the unsteady surface pressure near the trailing edge is computed and compared between the baseline and the two fence simulations. Both fences reduce γ^2 at low frequencies for normalized separation distances $\Delta z/c > P/c$. For these frequencies, both fences increase γ^2 in fence passages (i.e. for $\Delta z/c < P/c$) due to a 'channeling' effect from adjacent fence sidewalls. This increase is larger for the taller fence. The taller fence is louder than the shorter fence (but not the baseline) for low frequencies. This is hypothesized to be due to (a) increased γ^2 within fence passages, and (b) additional noise radiated by the leading edge of the taller fence as it is less aligned with the oncoming turbulence in the flow.

Acknowledgments

This research is funded by the National Science Foundation under grant number NSF/ CBET-1554196. Computational resources used for this research are provided by NSF XSEDE (Grant # TG-CTS130004) and the Argonne Leadership Computing Facility, which is a DOE Office of Science User Facility supported under Contract DE-AC02-06CH11357. Technical support for the FDL3DI software provided by Dr Daniel Garmann of Air Force Research Laboratory is acknowledged. The first author acknowledges the funding through the Wind Energy Science, Engineering, and Policy program at Iowa State.

ORCID iDs

Andrew Bodling https://orcid.org/0000-0002-1963-9467
Anupam Sharma https://orcid.org/0000-0002-8198-3891

References

[1] Brooks T F, Pope D S and Marcolini M A 1989 Airfoil self-noise and prediction *Technical Report* NASA RP 1218, NASA Langley Research Center
[2] Curle N 1955 The influence of solid boundaries upon aerodynamic sound *Proc. R. Soc.* A **231** 505–14
[3] Williams J E F and Hall L 1970 Aerodynamic sound generation by turbulent flow in the vicinity of a scattering half plane *J. Fluid Mech.* **40** 657–70
[4] Amiet R K 1976 Noise due to turbulent flow past a trailing edge *J. Sound Vib.* **47** 387–93
[5] Howe M S 1978 A review of the theory of trailing edge noise *J. Sound Vib.* **61** 437–65
[6] Oerlemans S, Sijtsma P and Mendez Lopez B 2007 Location and quantification of noise sources on a wind turbine *J. Sound Vib.* **299** 869–83
[7] Blake W K 1986 *Mechanics of Flow-Induced Sound and Vibration* vol 17 (New York: Academic)
[8] Lockard D P and Lilley G M 2004 The airframe noise reduction challenge *Technical Report* NASA/TM-2004-213013, NASA Langley Research Center

[9] Benyus J M 2002 *Biomimicry: Innovation Inspired by Nature* (New York: William Morrow Paperbacks)
[10] Solga A, Cerman Z, Striffler B F, Spaeth M and Barthlott W 2007 The dream of staying clean: lotus and biomimetic surfaces *Bioinspiration Biomimetics* **2** S126–34
[11] Korb J 2003 Thermoregulation and ventilation of termite mounds *Naturwissenschaften* **90** 212–9
[12] Graham R R 1934 The silent flight of owls *J. R. Aeronaut. Soc.* **38** 837–43
[13] Lilley G M 1998 A study of the silent flight of the owl *4th AIAA/CEAS Aeroacoustics Conf.* vol 2340 (American Institute of Aeronautics and Astronautics) pp l–6
[14] Bachmann T, Blazek S, Erlinghagen T, Baumgartner W and Wagner H 2012 *Barn Owl Flight* (Berlin: Springer) pp 101–17
[15] Kroeger R A, Grushka H D and Helvey T C 1972 Low speed aerodynamics for ultra-quiet flight *Technical Report* Wright-Patterson Air Force Base
[16] Sandberg R D and Jones L E 2011 Direct numerical simulations of low reynolds number flow over airfoils with trailing-edge serrations *J. Sound Vib.* **330** 3818–31
[17] Roger M, Schram C and De Santana L 2013 Reduction of airfoil turbulence-impingement noise by means of leading-edge serrations and/or porous material *19th AIAA/CEAS Aeroacoustics Conf.* (American Institute of Aeronautics and Astronautics)
[18] Agrawal B R and Sharma A 2016 Numerical analysis of aerodynamic noise mitigation via leading edge serrations for a rod–airfoil configuration *Int. J. Aeroacoustics* **15** 734–56
[19] Agrawal B R and Sharma A 2016 Numerical investigations of bio-inspired blade designs to reduce broadband noise in aircraft engines and wind turbines *2016 AIAA SciTech Meeting* (American Institute of Aeronautics and Astronautics)
[20] Oerlemans S, Fisher M, Maeder T and Kögler K 2009 Reduction of wind turbine noise using optimized airfoils and trailing-edge serrations *AIAA J.* **47** 1470–81
[21] Geyer T, Sarradj E and Fritzsche C 2010 Measurement of the noise generation at the trailing edge of porous airfoils *Exp. Fluids* **48** 291–308
[22] Jaworski J W and Peake N 2013 Aerodynamic noise from a poroelastic edge with implications for the silent flight of owls *J. Fluid Mech.* **723** 456–79
[23] Jaworski J W and Peake N 2013 Parametric guidance for turbulent noise reduction from poroelastic trailing edges and owls *19th AIAA/CEAS Aeroacoustics Conf.* (American Institute of Aeronautics and Astronautics)
[24] Clark I A, Devenport W, Jaworski J W, Daly C, Peake N and Glegg S 2014 Noise generating and suppressing characteristics of bio-inspired rough surfaces *20th AIAA/CEAS Aeroacoustics Meeting* (American Institute of Aeronautics and Astronautics)
[25] Finnigan J 2000 Turbulence in plant canopies *Ann. Rev. Fluid Mech.* **32** 519–71
[26] Clark I A, Alexander N W, Devenport W, Glegg S, Jaworski J W, Daly C and Peake N 2017 Bioinspired trailing-edge noise control *AIAA J.* **55** 740–54
[27] Bodling A, Agrawal B R, Sharma A, Clark I A, Alexander N W and Devenport W 2017 Numerical investigations of bio-inspired blade designs to reduce broadband noise in aircraft engines and wind turbines *55th AIAA Aerospace Sciences Meeting* (American Institute of Aeronautics and Astronautics)
[28] Bodling A, Agrawal B R, Sharma A, Clark I A, Alexander N W and Devenport W 2017 Numerical investigation of bio-inspired blade designs at high reynolds numbers for ultra-quiet aircraft and wind turbines *23rd AIAA/CEAS Aeroacoustics Conf.* (American Institute of Aeronautics and Astronautics)
[29] Bodling A and Sharma A 2017 Numerical investigation of noise reduction mechanisms in a bio-inspired airfoil *17th Int. Symp. on Transport Phenomena and Dynamics of Rotating Machinery*
[30] Visbal R M and Gaitonde V D 2002 On the use of higher-order finite-difference schemes on curvilinear and deforming meshes *J. Comput. Phys.* **181** 155–85
[31] Bodling A 2017 Numerical investigations of bio-inspired blade designs to reduce broadband noise in aircraft engines and wind turbines *Master's Thesis* Iowa State University
[32] Beam R M and Warming R F 1976 An implicit finite-difference algorithm for hyperbolic systems in conservation-law form *J. Comput. Phys.* **22** 87–110
[33] Beam R M and Warming R F 1978 An implicit factored scheme for the compressible Navier–Stokes equations *AIAA J.* **16** 393–402
[34] Williams J E F and Hawkings D L 1969 Sound generation by turbulence and surfaces in arbitrary motion *Phil. Trans. R. Soc. A* **264** 321–42
[35] Sharma A and Chen H 2013 Prediction of aerodynamic tonal noise from open rotors *J. Sound Vib.* **332** 3832–45
[36] Bodling A and Sharma A 2018 Implementation of the Ffowcs Willaims–Hawkings equations: predicting the far field noise from airfoils while using boundary layer tripping mechanisms *ASME J.* under review
[37] Kato C and Ikegawa M 1991 Large eddy simulation of unsteady turbulent wake of a circular cylinder using the finite element method *Advances in Numerical Simulation of Turbulent Flows* vol **1** (Portland, OR: American Society of Mechanical Engineers) pp 49–56
[38] Visbal R M 2014 Numerical exploration of flow control for delay of dynamic stall on a pitching airfoil *32nd AIAA Applied Aerodynamics Conf.* (American Institute of Aeronautics and Astronautics)
[39] Georgiadis N J, Rizetta D P and Fureby C 2010 Large-eddy simulation: current capabilities, recommended practices and future research *AIAA J.* **48** 1772–84
[40] Suhs E N, Rogers E S and Dietz E W 2002 Pegasus 5: an automated pre-processor for overset-grid CFD *32nd AIAA Fluid Dynamics Conf.* (American Institute of Aeronautics and Astronautics)
[41] Clark I A, Alexander N W and Devenport W 2017 Bio-inspired finlets for the reduction of marine rotor noise *23rd AIAA/CEAS Aeroacoustics Conf.* (American Institute of Aeronautics and Astronautics)
[42] Drela M 1989 XFOIL: an analysis and design system for low Reynolds number airfoils *Low Reynolds Number Aerodynamics* (Berlin: Springer) pp 1–12
[43] Sagrado A G and Hynes T 2012 Wall pressure sources near an airfoil trailing edge under turbulent boundary layers *J. Fluids Struct.* **30** 3–34
[44] Gregory N and O'Reilly C L 1970 Low-speed aerodynamic characteristics of NACA 0012 aerofoil section, including the effects of upper-surface roughness simulating hoar frost *Technical Report* NASA Reports and Memoranda 3726
[45] Gravante S P, Naguib A M, Wark C E and Nagib H M 1998 Characterization of the pressure fluctuations under a fully developed turbulent boundary layer *AIAA J.* **36** 1808–16
[46] Lee H and Kang S H 2000 Flow characteristics of transitional boundary layers on an airfoil in wakes *ASME J. Fluids Eng.* **122** 522–32
[47] Nagib H M and Chauhan K A 2008 Variations of von Kármán coefficient in canonical flows *Phys. Fluids* **20** 101518
[48] Wolf W R, Azevedo J L F and Lele S K 2012 Convective effects and the role of quadrupole sources for aerofoil aeroacoustics *J. Fluid Mech.* **708** 502–38
[49] Welch P 1967 The use of fast fourier transform for the estimation of power spectra: a method based on time averaging over short, modified periodograms *IEEE Trans. Audio Electroacoust.* **15** 70–3
[50] Afshari A, Azarpeyvand M, Dehghan A A and Szőke M 2016 Trailing edge noise reduction using novel surface treatments *22nd AIAA/CEAS Aeroacoustics Conf.* (American Institute of Aeronautics and Astronautics)
[51] Clark I A, Devenport W and Alexander N W 2017 Understanding trailing edge noise control using finlets *AIAA J.* (under review)
[52] Amiet R K 1975 Acoustic radiation from an airfoil in a turbulent stream *J. Sound Vib.* **41** 407–20